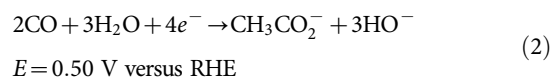
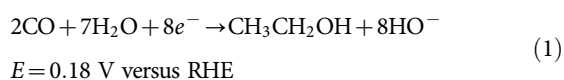


Electroreduction of carbon monoxide to liquid fuel on oxide-derived nanocrystalline copper

Christina W. Li¹, Jim Ciston² & Matthew W. Kanan¹

The electrochemical conversion of CO₂ and H₂O into liquid fuel is ideal for high-density renewable energy storage and could provide an incentive for CO₂ capture. However, efficient electrocatalysts for reducing CO₂ and its derivatives into a desirable fuel^{1–3} are not available at present. Although many catalysts^{4–11} can reduce CO₂ to carbon monoxide (CO), liquid fuel synthesis requires that CO is reduced further, using H₂O as a H⁺ source. Copper (Cu) is the only known material with an appreciable CO electroreduction activity, but in bulk form its efficiency and selectivity for liquid fuel are far too low for practical use. In particular, H₂O reduction to H₂ outcompetes CO reduction on Cu electrodes unless extreme overpotentials are applied, at which point gaseous hydrocarbons are the major CO reduction products^{12,13}. Here we show that nanocrystalline Cu prepared from Cu₂O ('oxide-derived Cu') produces multi-carbon oxygenates (ethanol, acetate and *n*-propanol) with up to 57% Faraday efficiency at modest potentials (–0.25 volts to –0.5 volts versus the reversible hydrogen electrode) in CO-saturated alkaline H₂O. By comparison, when prepared by traditional vapour condensation, Cu nanoparticles with an average crystallite size similar to that of oxide-derived copper produce nearly exclusive H₂ (96% Faraday efficiency) under identical conditions. Our results demonstrate the ability to change the intrinsic catalytic properties of Cu for this notoriously difficult reaction by growing interconnected nanocrystallites from the constrained environment of an oxide lattice. The selectivity for oxygenates, with ethanol as the major product, demonstrates the feasibility of a two-step conversion of CO₂ to liquid fuel that could be powered by renewable electricity.

Cu electrodes have been thoroughly evaluated in both CO₂ (refs 7, 14, 15) and CO reduction^{12,13,16,17} electrolyses. In CO₂-saturated aqueous solutions, polycrystalline Cu foil produces a mixture of compounds that are dominated by H₂ at low overpotential, by CO and HCO₂[–] at high overpotential and by hydrocarbons and multi-carbon oxygenates at the most extreme potentials^{18,19}. When supplied with CO in the absence of CO₂, Cu produces hydrocarbons and multi-carbon oxygenates, but very negative potentials are still required to promote CO reduction over H₂ evolution^{12,13}. Large overpotentials preclude energetically efficient electrolysis and favour hydrocarbons over liquid oxygenates. We recently discovered that oxide-derived Cu (OD-Cu) has much higher selectivity for CO₂ electroreduction over H₂ evolution than does polycrystalline Cu (ref. 20). Because CO reduction activity may be obscured in the presence of a large excess of CO₂, we questioned whether OD-Cu would reduce CO with greater efficiency than other Cu materials when supplied with CO directly. Here we show that OD-Cu reduces CO with high Faraday efficiency at an overpotential >0.6 V lower than that of polycrystalline Cu foil. This improvement results both from an increase in the intrinsic CO reduction activity and from a decrease in intrinsic H₂O reduction activity on OD-Cu. The major CO reduction products are ethanol and acetate, which correspond to 8e[–] and 4e[–] reductions with H₂O as the H⁺ source (equations (1) and (2), where *E* is the equilibrium potential).



By comparing OD-Cu to electrodes comprised of commercial Cu nanoparticles, we show that CO reduction activity is not a consequence of nanocrystallite size or morphology; instead, we propose that grain boundaries participate in the catalysis.

OD-Cu electrodes were prepared by annealing polycrystalline Cu foil in air at 500 °C to grow a thick Cu₂O layer on the surface and subsequently reducing this oxide to form Cu⁰ nanocrystallites. We used two reduction methods to vary the properties of the material. To obtain OD-Cu 1, the Cu₂O precursor was reduced electrochemically in aqueous solution at ambient temperature. This procedure had previously been found to yield nanocrystalline Cu with maximal selectivity for CO₂ reduction²⁰. To obtain OD-Cu 2, the Cu₂O precursor was reduced with H₂ at 130 °C. The OD-Cu electrodes were compared to commercial Cu nanoparticles that had been synthesized by vapour condensation. Cu nanoparticle electrodes were prepared by drop-casting suspensions of the nanoparticles and fluorinated binder onto metal substrates.

All three types of electrodes exhibited similar morphologies when imaged by scanning electron microscopy (SEM) (Fig. 1a, d, g). Particle sizes ranged from about 30 nm to 100 nm, and the particles formed aggregated films. Low-resolution transmission electron microscopy (TEM) confirmed the range of particle sizes observed via SEM (Fig. 1b, e, h). High-resolution TEM of OD-Cu 1 and OD-Cu 2 showed interconnected nanocrystalline networks with distinct grain boundaries between nanocrystallites (Fig. 1f, i). In contrast, the Cu nanoparticle electrode appeared as an aggregation of overlapping particles (Fig. 1c). Differential capacitance measurements yielded electrochemical roughness factors of 135, 48 and 26 for OD-Cu 1, OD-Cu 2 and the Cu nanoparticle electrode, respectively (Extended Data Fig. 5 and Extended Data Table 2). X-ray photoelectron spectroscopy indicated that the surfaces were comprised of both Cu⁰ and Cu₂O, the latter resulting from air exposure during the X-ray photoelectron spectroscopy sample preparation (Extended Data Figs 1, 2 and 3). Grazing incidence X-ray diffraction patterns for all of the electrodes exhibited peaks at the expected positions for an ideal Cu lattice, indicating no uniform expansion or compression of the unit cell (Fig. 1j, k, l). The patterns differed substantially in their peak widths, however. Using the Scherrer equation, both OD-Cu 2 and the Cu nanoparticle electrode exhibited average crystallite sizes ⟨*D*⟩ > 100 nm, while OD-Cu 1 had a smaller ⟨*D*⟩ of 31 nm. Additional high-resolution grazing incidence X-ray diffraction patterns were collected for OD-Cu 1 and OD-Cu 2 with synchrotron radiation to determine the amount of microstrain in each sample using Williamson–Hall analysis. This analysis yielded microstrain values of 0.2% and 0.05% for OD-Cu 1 and OD-Cu 2, respectively (Extended Data Fig. 4).

CO electroreduction activity was measured under steady-state conditions by performing constant-potential electrolyses for multiple hours in 0.1 M KOH saturated with 1 atm of CO at ambient temperature. The concentration of CO in solution is only 1 mM under these conditions. Solution-phase and gas-phase products were quantified by nuclear magnetic

¹Department of Chemistry, Stanford University, Stanford 94305, California. ²National Center for Electron Microscopy, Lawrence Berkeley National Laboratory, Berkeley 94720, California.

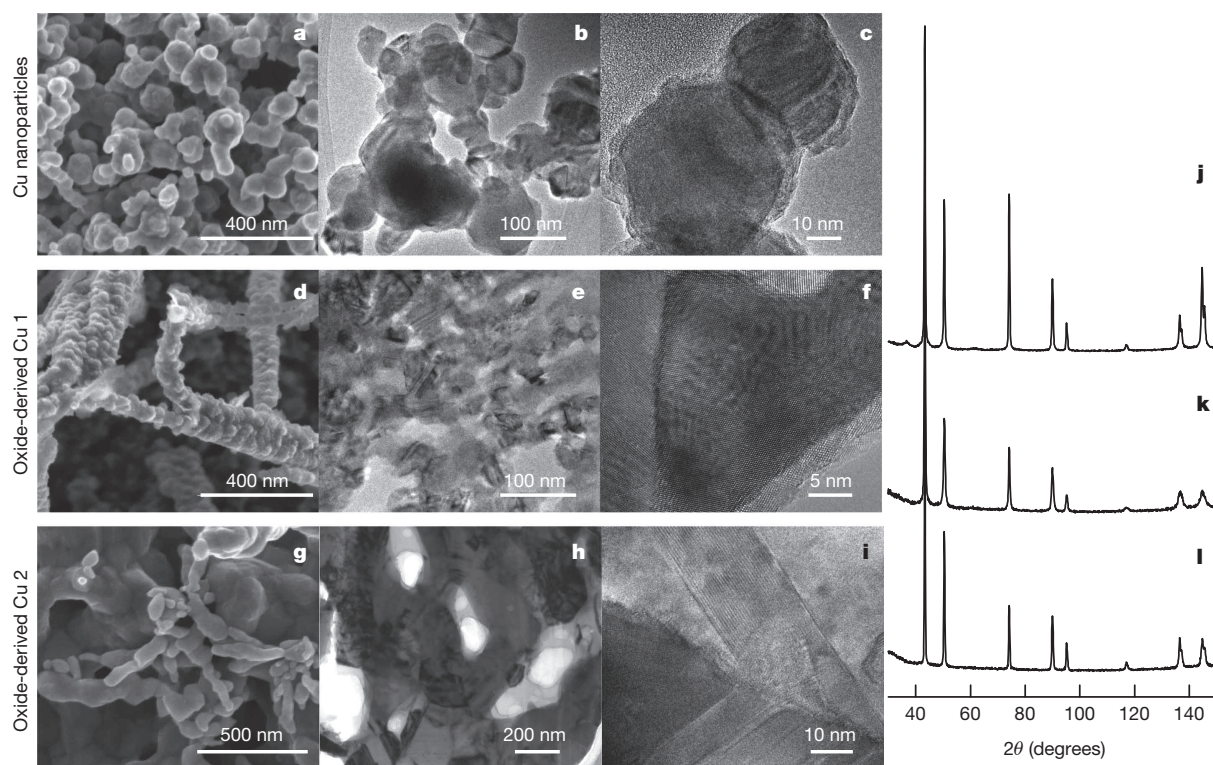


Figure 1 | Physical characterization of Cu nanoparticle and OD-Cu electrodes. Top row, the Cu nanoparticle electrode. Middle row, the OD-Cu 1 electrode. Bottom row, the OD-Cu 2 electrode. **a, d, g**, SEM images. **b, e, h**, Low-magnification TEM images. **c, f, i**, High-resolution TEM images. **j, k, l**, Grazing incidence X-ray diffraction patterns.

resonance (NMR) spectroscopy and gas chromatography, respectively. Electrolyses were performed at a range of applied potentials E between -0.25 V and -0.5 V versus the reversible hydrogen electrode (RHE). The modest reducing potential and low CO concentration provides a stringent test of a catalyst's selectivity for CO versus H_2O reduction. Under these conditions, polycrystalline Cu foil exhibited low geometric current densities and H_2 was the only detectable product. These results are consistent with previous results in KOH, in which much more negative potentials (-0.7 V versus RHE) and a high flow rate of CO through the solution were required to attain 22% total Faraday efficiency for CO reduction, with only 7% Faraday efficiency for oxygenates¹³. A maximum CO reduction Faraday efficiency of 65% was reported for polycrystalline Cu foil at -0.9 V versus RHE in a mixed KCl and KHCO_3 electrolyte, although only 10% Faraday efficiency corresponded to the formation of oxygenates¹².

Larger geometric current densities were obtained with OD-Cu and Cu nanoparticle electrodes as a result of their roughness factors, which facilitated product quantification and comparison of their selectivities (Fig. 2 and Extended Data Table 1). For the Cu nanoparticle electrode, the Faraday efficiency for H_2 was $\geq 94\%$ at all potentials examined; the small remainder of the current corresponded to acetate, ethanol and ethylene formation. The high selectivity for H_2O reduction on this electrode mimics that of a Cu foil electrode. In contrast, OD-Cu electrodes had a much greater propensity for CO reduction. OD-Cu 1 attained a total CO reduction Faraday efficiency of 57% at -0.3 V, whereas OD-Cu 2 attained 48% at -0.4 V. These values declined at more negative potentials, but this decline was simply the result of the catalysts reaching the mass-transport-limited current density for CO reduction (see below). For both materials, ethanol and acetate were the nearly exclusive CO reduction products at the more positive potentials, whereas ethylene production emerged at more negative potentials. OD-Cu 2 also produced substantial amounts of propanol, which was only observed for OD-Cu 1 under higher CO pressure (see below). In addition to the reduction products, OD-Cu electrodes also produced small amounts of formate, the product of CO hydration.

b, e, h, Low-magnification TEM images. **c, f, i**, High-resolution TEM images. **j, k, l**, Grazing incidence X-ray diffraction patterns.

The higher Faraday efficiency for CO reduction on OD-Cu electrodes compared to a Cu nanoparticle electrode reflected higher intrinsic CO reduction activity. Figure 2b and c shows the geometric and surface-area-normalized current densities for CO reduction (j_{COredn}) versus E for the three electrodes. The difference in intrinsic activity between two electrodes corresponds to the ratio of their normalized current densities in the absence of mass-transport contributions to the kinetics. The rate of CO transport from bulk solution through the diffusion layer to the electrode surface determines the maximum attainable geometric j_{COredn} (ref. 21). The Cu nanoparticle electrode did not reach a mass-transport limit between -0.3 V and -0.5 V, as shown by the exponential increase in j_{COredn} across this potential range. Its Tafel slope was 112 mV dec^{-1} (where 'dec' means decade, or one order of magnitude). On account of their higher activity, the geometric j_{COredn} on OD-Cu electrodes quickly reached a plateau value of 0.5 mA cm^{-2} as the overpotential was increased (Fig. 2b), indicating that this value is approximately the mass transport limit with only 1 mM CO in solution. At -0.3 V, before the onset of the mass transport contributions, normalized j_{COredn} was 23-fold higher for OD-Cu 1 and 43-fold higher for OD-Cu 2 than for the Cu nanoparticle electrode (Fig. 2c). To determine the dependence of j_{COredn} on E for OD-Cu electrodes in the absence of mass-transport effects, additional electrolyses were performed in the range $-0.25 \text{ V} > E > -0.35 \text{ V}$ (Extended Data Fig. 8). A Tafel slope of approximately 113 mV dec^{-1} was obtained.

The electrodes also differed in their intrinsic activities for H_2O reduction. Figure 2d and e shows the normalized current density for H_2O reduction (j_{H_2}) in CO-saturated and N_2 -saturated 0.1 M KOH, respectively. All three electrodes exhibited an H_2O reduction activity 2-fold to 5-fold lower in the presence of CO than in the presence of N_2 , indicating some poisoning of the sites for H_2O reduction by CO binding²². In CO-saturated electrolyte, normalized j_{H_2} was similar for the Cu nanoparticle electrode and OD-Cu 2, but was 2-fold to 6-fold lower for OD-Cu 1. The suppression of H_2O reduction contributes to the higher Faraday efficiency for CO reduction on OD-Cu 1. In N_2 -saturated electrolyte, j_{H_2} was suppressed 4–8-fold on OD-Cu 1 and 2–6-fold on OD-Cu 2

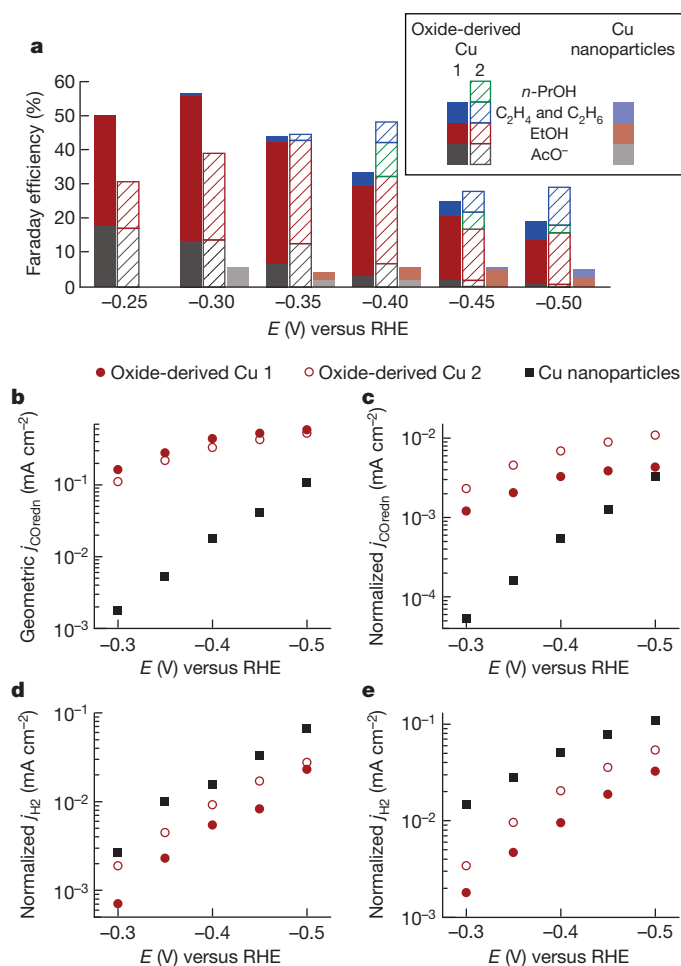


Figure 2 | Comparison between OD-Cu 1, OD-Cu 2 and Cu nanoparticle electrodes in electrolyses performed in 0.1 M KOH saturated with 1 atm CO at ambient temperature. **a**, Faraday efficiencies for CO reduction products ethanol (EtOH), acetate (AcO⁻), *n*-propanol (*n*-PrOH), ethylene (C₂H₄) and ethane (C₂H₆) at selected potentials versus the reversible hydrogen electrode. The remaining Faraday efficiency in all cases corresponds to H₂ evolution. The current density for the Cu nanoparticle electrode at -0.25 V was too low for product quantification. **b**, Geometric current densities for CO reduction. **c**, Surface-area-normalized current densities for CO reduction. **d**, Surface-area-normalized current density for H₂ evolution under 1 atm of CO. **e**, Surface-area-normalized current density for H₂ evolution under 1 atm of N₂.

compared to the Cu nanoparticle electrode. The similar Tafel slopes for H₂ evolution suggest that OD-Cu electrodes have a lower density of active sites for this reaction.

To confirm that the geometric j_{COredn} at 1 atm CO is limited by the kinetics of CO mass transport, OD-Cu 1 was evaluated in an electrolysis performed in 0.1 M KOH saturated with 2.4 atm of CO. At potentials between -0.3 V and -0.5 V, geometric j_{COredn} was 1.8–2.4-fold higher under these conditions (Fig. 3a). The Faraday efficiency for CO reduction at $E < -0.3$ V was also substantially improved (Fig. 3b). These results indicate that practical current densities may be possible in this moderate overpotential regime by further increasing CO transport to the catalyst.

The electrolysis data provide some insight into the mechanism of CO reduction on OD-Cu. The j_{COredn} Tafel slope is consistent with a rate-limiting initial $1e^-$ transfer to CO. The absence of C1 products indicates that C–C coupling is rapid once the process of CO reduction initiates²³ or that the initial e^- transfer is coupled to C–C bond formation between a surface-bound CO and a CO from solution¹⁶. The latter would account for increased j_{COredn} at increased pressure if the active sites of OD-Cu were saturated with CO at 1 atm (refs 24, 25). The formation of acetate probably arises from attack of HO⁻ on a surface-bound ketene or

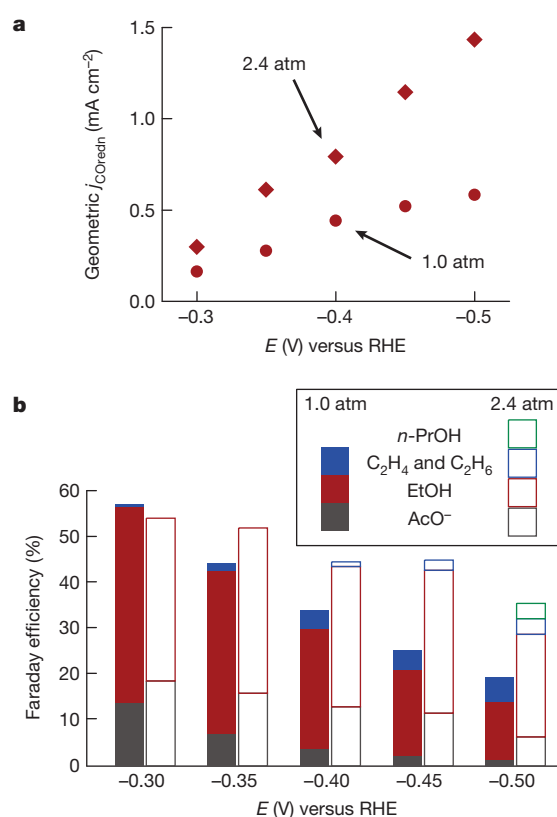


Figure 3 | Comparison of CO reduction in 0.1 M KOH saturated with 1 atm of CO versus 2.4 atm of CO. **a**, Geometric current densities for CO reduction. **b**, Faraday efficiencies for CO reduction products at selected potentials.

other carbonyl-containing intermediate after C–C bond formation has occurred. This contention is supported by the observation of substantially increased acetate formation when the electrolysis is performed in 1 M KOH (Extended Data Fig. 9).

The results above implicate the participation of grain boundary surfaces in the CO reduction catalysis on OD-Cu. Although OD-Cu 1 and OD-Cu 2 differ in their bulk properties, both are distinguished from Cu nanoparticle electrodes by having a high density of grain boundaries as a consequence of their formation from a solid phase. Given that grain boundaries can support surface structures that are not stable on an individual nanocrystal²⁶, the enhanced CO reduction activity on OD-Cu electrodes relative to Cu nanoparticle electrodes is consistent with the presence of highly active sites on their grain boundary surfaces. The difference in their product distribution could reflect differences in grain boundary structures resulting from electrochemical versus H₂ reduction of Cu₂O. The results suggest that engineering the grain boundaries by altering the oxide reduction method or by using an alternative preparation of nanocrystalline materials could yield catalysts with higher activity and selectivity for long-chain products. The participation of grain boundary surfaces in catalysis has previously been proposed to explain correlations between grain boundary density and methanol electrooxidation activity with Pt nanoparticles²⁷ and PtRu alloy nanoparticles²⁸.

Catalytic processes have been optimized over the past century to reduce CO with H₂ to alkanes, methanol or higher alcohols. Although many of these processes are efficient, they all require high temperatures and pressures (typically 250–400 °C and 50–150 atm) and large-scale reactors that are poorly matched to diffuse renewable energy sources^{29,30}. Moreover, H₂ is almost exclusively derived from fossil fuel sources at present. Electrolytic syntheses enabled by the catalysis described here could provide a more direct, versatile and energetically efficient route to distributed liquid fuel production powered by renewable energy.

METHODS SUMMARY

CO reduction electrolyses were performed in CO-saturated 0.1 M KOH electrolyte in a two-compartment electrochemical cell. The headspace of the cathodic chamber was continuously purged with CO into the sampling loop of a gas chromatograph to enable periodic quantification of the gas-phase products. The solution-phase products were quantified by NMR analysis of the electrolyte at the conclusion of the electrolyses. OD-Cu electrodes were prepared by electropolishing pieces of polycrystalline Cu foil (99.9999%) in 85% phosphoric acid and subsequently annealing the electrodes in air at 500 °C for 1 h to form a thick Cu₂O layer. The active OD-Cu 1 layer was formed *in situ* at the beginning of CO reduction electrolysis, requiring 10–12 C cm⁻² of charge to fully reduce the Cu₂O material. OD-Cu 2 was formed by reduction of the Cu₂O layer in flowing H₂ at 130 °C for 2 h.

Online Content Any additional Methods, Extended Data display items and Source Data are available in the online version of the paper; references unique to these sections appear only in the online paper.

Received 20 June 2013; accepted 27 January 2014.

Published online 9 April 2014.

- Appel, A. M. *et al.* Frontiers, opportunities, and challenges in biochemical and chemical catalysis of CO₂ fixation. *Chem. Rev.* **113**, 6621–6658 (2013).
- Jhong, H. R., Ma, S. & Kenis, P. J. A. Electrochemical conversion of CO₂ to useful chemicals: current status, remaining challenges, and future opportunities. *Curr. Opin. Chem. Eng.* **2**, 191–199 (2013).
- Cole, E. B. & Bocarsly, A. B. in *Carbon Dioxide as Chemical Feedstock* (ed. Aresta, M.) 291–316 (Wiley, 2010).
- Costentin, C., Robert, M. & Saveant, J. M. Catalysis of the electrochemical reduction of carbon dioxide. *Chem. Soc. Rev.* **42**, 2423–2436 (2013).
- Benson, E. E., Kubiak, C. P., Sathrum, A. J. & Smieja, J. M. Electrocatalytic and homogeneous approaches to conversion of CO₂ to liquid fuels. *Chem. Soc. Rev.* **38**, 89–99 (2009).
- Costentin, C., Drouet, S., Robert, M. & Saveant, J. M. A local proton source enhances CO₂ electroreduction to CO by a molecular Fe catalyst. *Science* **338**, 90–94 (2012).
- Hori, Y. in *Modern Aspects of Electrochemistry* Vol. 42 (eds Vayenas, C. G., White, R. E. & Gamboa-Aldeco, M. E.) 89–189 (Springer, 2008).
- Chen, Y., Li, C. W. & Kanan, M. W. Aqueous CO₂ reduction at very low overpotential on oxide-derived Au nanoparticles. *J. Am. Chem. Soc.* **134**, 19969–19972 (2012).
- Tornow, C. E., Thorson, M. R., Ma, S., Gewirth, A. A. & Kenis, P. J. A. Nitrogen-based catalysts for the electrochemical reduction of CO₂ to CO. *J. Am. Chem. Soc.* **134**, 19520–19523 (2012).
- DiMeglio, J. L. & Rosenthal, J. Selective conversion of CO₂ to CO with high efficiency using an inexpensive bismuth-based electrocatalyst. *J. Am. Chem. Soc.* **135**, 8798–8801 (2013).
- Ebbesen, S. D. & Mogensén, M. Electrolysis of carbon dioxide in solid oxide electrolysis cells. *J. Power Sources* **193**, 349–358 (2009).
- Hori, Y., Takahashi, R., Yoshinami, Y. & Murata, A. Electrochemical reduction of CO at a copper electrode. *J. Phys. Chem. B* **101**, 7075–7081 (1997).
- Hori, Y., Murata, A., Takahashi, R. & Suzuki, S. Electroreduction of CO to CH₄ and C₂H₄ at a copper electrode in aqueous solutions at ambient temperature and pressure. *J. Am. Chem. Soc.* **109**, 5022–5023 (1987).
- Gattrell, M., Gupta, N. & Co, A. A review of the aqueous electrochemical reduction of CO₂ to hydrocarbons at copper. *J. Electroanal. Chem.* **594**, 1–19 (2006).
- Hori, Y., Takahashi, I., Koga, O. & Hoshi, N. Selective formation of C₂ compounds from electrochemical reduction of CO₂ at a series of copper single crystal electrodes. *J. Phys. Chem. B* **106**, 15–17 (2002).
- Calle-Vallejo, F. & Koper, M. T. M. Theoretical considerations on the electroreduction of CO to C₂ species on Cu(100) electrodes. *Angew. Chem. Int. Ed.* **52**, 7282–7285 (2013).
- Schouten, K. J. P., Qin, Z. S., Gallent, E. P. & Koper, M. T. M. Two pathways for the formation of ethylene in CO reduction on single-crystal copper electrodes. *J. Am. Chem. Soc.* **134**, 9864–9867 (2012).
- Kuhl, K. P., Cave, E. R., Abram, D. N. & Jaramillo, T. F. New insights into the electrochemical reduction of carbon dioxide on metallic copper surfaces. *Energy Environ. Sci.* **5**, 7050–7059 (2012).
- Hori, Y., Murata, A. & Takahashi, R. Formation of hydrocarbons in the electrochemical reduction of carbon dioxide at a copper electrode in aqueous solution. *J. Chem. Soc. Faraday Trans. 1* **85**, 2309–2326 (1989).
- Li, C. W. & Kanan, M. W. CO₂ reduction at low overpotential on Cu electrodes resulting from the reduction of thick Cu₂O films. *J. Am. Chem. Soc.* **134**, 7231–7234 (2012).
- Gileadi, E. *Electrode Kinetics for Chemists, Engineers, and Materials Scientists* Ch. 1 1–8 (Wiley, 1993).
- Hori, Y., Murata, A. & Yoshinami, Y. Adsorption of CO, intermediately formed in electrochemical reduction of CO₂, at a copper electrode. *J. Chem. Soc. Faraday Trans. 87*, 125–128 (1991).
- Montoya, J. H., Peterson, A. A. & Nørskov, J. K. Insights into C–C coupling in CO₂ electroreduction on copper electrodes. *ChemCatChem* **5**, 737–742 (2013).
- Koga, O. *et al.* Infrared spectroscopic and voltammetric study of adsorbed CO on stepped surfaces of copper monocrystalline electrodes. *Electrochim. Acta* **50**, 2475–2485 (2005).
- Shaw, S. K. *et al.* Role of axially coordinated surface sites for electrochemically controlled carbon monoxide adsorption on single crystal copper electrodes. *Phys. Chem. Chem. Phys.* **13**, 5242–5251 (2011).
- Radetic, T., Lancon, F. & Dahmen, U. Chevron defect at the intersection of grain boundaries with free surfaces in Au. *Phys. Rev. Lett.* **89**, 085502 (2002).
- Wang, S. Y., Jiang, S. P., White, T. J., Guo, J. & Wang, X. Electrocatalytic activity and interconnectivity of Pt nanoparticles on multiwalled carbon nanotubes for fuel cells. *J. Phys. Chem. C* **113**, 18935–18945 (2009).
- Gavrilov, A. N. *et al.* On the influence of the metal loading on the structure of carbon-supported PtRu catalysts and their electrocatalytic activities in CO and methanol electrooxidation. *Phys. Chem. Chem. Phys.* **9**, 5476–5489 (2007).
- Mills, G. A. Status and future opportunities for conversion of synthesis gas to liquid fuels. *Fuel* **73**, 1243–1279 (1994).
- Gupta, M., Smith, M. L. & Spivey, J. J. Heterogeneous catalytic conversion of dry syngas to ethanol and higher alcohols on Cu-based catalysts. *ACS Catal.* **1**, 641–656 (2011).

Acknowledgements We thank Stanford University and the NSF (CHE-1266401) for support of this work. C.W.L. gratefully acknowledges an NSF Predoctoral Fellowship. A portion of this work was performed at NCEM, which is supported by the Office of Science, Office of Basic Energy Sciences of the US Department of Energy under contract number DE-AC02-05CH11231. We thank M. Toney and B. Shyam for assistance with grazing incidence X-ray diffraction performed at SSRL, a national user facility operated by Stanford University on behalf of the Office of Basic Energy Sciences of the US Department of Energy.

Author Contributions C.W.L. and M.W.K. designed the experiments. C.W.L. prepared and characterized all electrodes and performed all electrochemical experiments; J.C. obtained all TEM images; C.W.L. and M.W.K. wrote the manuscript. All authors contributed to the overall scientific interpretation and edited the manuscript.

Author Information Reprints and permissions information is available at www.nature.com/reprints. The authors declare competing financial interests: details are available in the online version of the paper. Readers are welcome to comment on the online version of the paper. Correspondence and requests for materials should be addressed to M.W.K. (mkanan@stanford.edu).

METHODS

Materials. Potassium hydroxide (semiconductor grade, 99.99%) and HClO_4 (67–72% in water) were purchased from Sigma Aldrich; *ortho*-phosphoric acid (85% in water) was purchased from Fisher Scientific; carbon monoxide (99.9%) and H_2 (99.9%) were purchased from Praxair; copper foil (99.9999%, 0.1 mm thick) was purchased from Alfa Aesar; copper wire (99.9%, 0.020 inch diameter) was purchased from McMaster; Cu nanoparticles (99.9%, 40 nm) were purchased from US Research Nanomaterials. All chemicals were used without further purification. Electrolyte solutions were prepared with deionized water (Ricca Chemical, ASTM Type I).

Preparation of oxide-derived Cu 1. Copper foils were first electropolished in 85% *ortho*-phosphoric acid at 4 V versus a titanium counter electrode for 5 min. After rinsing with deionized water and drying under a stream of N_2 , foils were placed in a muffle furnace (Thermo Scientific) under an air atmosphere at 500 °C for 1 h. Electrodes were then allowed to cool slowly to room temperature over several hours. The active oxide-derived Cu material was formed *in situ* during CO reduction electrolysis. Typically, 10–12 C cm^{-2} at about 7.5 mA cm^{-2} were passed to fully reduce the Cu_2O layer.

Preparation of oxide-derived Cu 2. Copper oxide electrodes were prepared at 500 °C as described above. Instead of electrolytic reduction of the Cu_2O layer, electrodes were reduced under an H_2 atmosphere. Oxidized electrodes were placed in a tube furnace (Thermo Scientific) with flowing H_2 at 100 $\text{cm}^3 \text{min}^{-1}$ (standard cubic centimeters per minute) and heated at 130 °C for 2 h.

Preparation of Cu nanoparticle electrodes. 100 mg of commercially available Cu nanoparticle powder, prepared by a wire electrical explosion method (99.9%, 40 nm, US Nanomaterials), was ground in a mortar and pestle with 10 mg of polyvinylidene fluoride to form a uniform powder. This powder was suspended in 10 ml of isopropanol and sonicated for 1 h. 200 μl of the Cu nanoparticle suspension was drop-dried onto a 2- cm^2 Cu foil that had been etched for 30 s in 50% HNO_3 and rinsed in deionized water. The isopropanol was allowed to evaporate slowly at room temperature. A Cu wire was subsequently attached to the back side using Ag epoxy to make electrical contact and covered with insulating epoxy to protect it from the solution during electrolysis.

Electrochemical measurements. A CH Instruments 760D or 660D potentiostat was used for all experiments. A piece of platinum gauze (Sigma, 99.9%) was used as the counter electrode. The electrolyte used for all CO reduction experiments was 0.1 M KOH saturated with CO with a pH of 13. Potentials E were measured against an Hg/HgO reference (1.0 M KOH, Koslow Scientific) or an Ag/AgCl reference electrode (3.0 M KCl, World Precision Instruments or BASi) and converted to the RHE reference scale using:

$$E(\text{versus RHE}) = E(\text{versus Hg/HgO}) + 0.140 \text{ V} + 0.0591 \text{ V} \times \text{pH}$$

$$E(\text{versus RHE}) = E(\text{versus Ag/AgCl}) + 0.210 \text{ V} + 0.0591 \text{ V} \times \text{pH}$$

CO reduction electrolyses and product analysis. Ambient pressure electrolyses were performed in a two-compartment electrochemical cell sealed to be gas-tight with silicone stoppers. A piece of Selemion anion exchange membrane was used as the separator. Each compartment contained 20 ml of 0.1 M KOH electrolyte. The solution in the cathodic compartment was purged with CO for 20 min before the start of electrolysis. The headspace of the cathodic compartment was approximately 5 ml. CO gas was delivered into the cathodic compartment at a rate of 5.00 $\text{cm}^3 \text{min}^{-1}$ and vented directly into the gas-sampling loop of a gas chromatograph (SRI Instruments).

High-pressure electrolyses were performed in a modified two-compartment electrochemical cell, in which a glass cap was clamped to the cathodic chamber with an O-ring seal. A piece of Selemion anion exchange membrane was used as the separator. Each compartment contained 30 ml of 0.1 M KOH electrolyte. A bleed valve was placed at the gas outlet of the cathodic compartment, which allowed control of the gas pressure while still permitting flow of gas out of the cell. The solution in the cathodic compartment was purged with CO before the start of electrolysis until the desired pressure of 2.4 bar \pm 0.07 bar was achieved. CO gas was delivered into the cathodic compartment at a rate of 10.0 $\text{cm}^3 \text{min}^{-1}$ and vented directly into the gas-sampling loop of a gas chromatograph (SRI Instruments).

A gas chromatograph run was initiated every 30 min. The gas chromatograph was equipped with a packed MolSieve 5A column and a packed HaySep D column. Argon (Praxair, 99.999%) was used as the carrier gas. A flame ionization detector with methanizer was used to quantify C_2H_4 and C_2H_6 concentration and a thermal conductivity detector was used to quantify H_2 concentration. The partial current density of ethylene production $j_{\text{C}_2\text{H}_4}$ was calculated from the gas chromatograph peak area as follows:

$$j_{\text{C}_2\text{H}_4} = \frac{\text{Peak area}}{\alpha} \times \text{Flow rate} \times \frac{2Fp_0}{RT} \times \frac{1}{\text{Electrode area}}$$

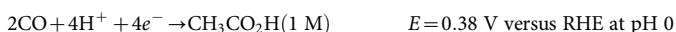
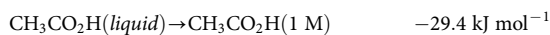
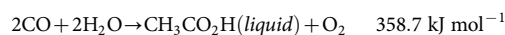
where α is a conversion factor based on calibration of the gas chromatograph with a standard sample, $p_0 = 1.013$ bar, R is the gas constant, F is Faraday's constant and $T = 273.15$ K.

Ethanol (EtOH), acetate (AcO^-) and *n*-propanol (*n*- PrOH) concentrations were analysed on a Varian Inova 600-MHz NMR spectrometer. A 0.5-ml sample of the electrolyte was mixed with 0.1 ml D_2O and 1.67 parts per million (by mass fraction) dimethyl sulphoxide (Sigma, 99.99%) was added as an internal standard. The one-dimensional ^1H spectrum was measured with water suppression using a presaturation method (see Extended Data Fig. 7).

Activity versus potential plots. Each point in the Faraday efficiency and current density versus potential plots (Fig. 2 and Fig. 3) was obtained by a separate electrolysis with a freshly prepared electrode. Not all potential points were repeated, but for those in which multiple repeats were run, the Faraday efficiency and current density did not vary by more than $\pm 10\%$. In the ambient pressure experiments with OD-Cu 1 electrodes, the electrode was first held at -0.5 V versus RHE for 45 min to reduce the Cu_2O layer. An aliquot was taken at the end of this period, and the potential was then stepped to the indicated value (see Extended Data Fig. 6). Partial current densities for C_2H_4 , C_2H_6 and H_2 production were calculated from the gas chromatograph spectra every 30 min and averaged over 2–3 h. In the high-pressure experiments, the Cu_2O layer was reduced at the same potential as the subsequent bulk electrolysis, and the charge for oxide reduction was estimated by taking the charge passed in the initial plateau period until the current fell below 5 mA cm^{-2} . In the H_2 Tafel experiments under N_2 , stepped electrolyses were run using a single electrode for all potential points. In addition, the Tafel data under CO for OD-Cu 2 (Extended Data Fig. 8a) was also collected using stepped electrolysis, in which the H_2 partial current density was calculated from gas chromatograph spectra every 12 min and subtracted from the total current density to give the partial current density for CO reduction.

Surface-area-normalized current densities for OD-Cu 1, OD-Cu 2 and Cu nanoparticle electrodes (Fig. 2c, d and e) were obtained by dividing the geometric current densities by the electrode roughness factors. For OD-Cu 1, the roughness factor used was 135, and for OD-Cu 2, the roughness factor used was 48, which are average values of the roughness factors measured after 1 h and after 12 h of bulk electrolysis.

Equilibrium potentials. Equilibrium potentials for the half reactions of CO to acetate and CO to ethanol were calculated from tabulated values of the standard molar Gibbs energy of formation at 298.15 K (ref. 32) as in the example below. The calculation assumes that gases are at 1 atm and liquids are in their pure form.



applying the Nernst equation:

$$E = 0.38 \text{ V} - \frac{RT}{4F} \ln \left[\frac{a_{\text{CH}_3\text{CO}_2\text{H}}}{(a_{\text{H}^+})^4} \right] + 0.059 \text{ V} \times \text{pH} = 0.50 \text{ V versus RHE at pH 13,}$$

where $a_{\text{CH}_3\text{CO}_2\text{H}}$ is the activity of acetic acid and a_{H^+} is the proton activity.

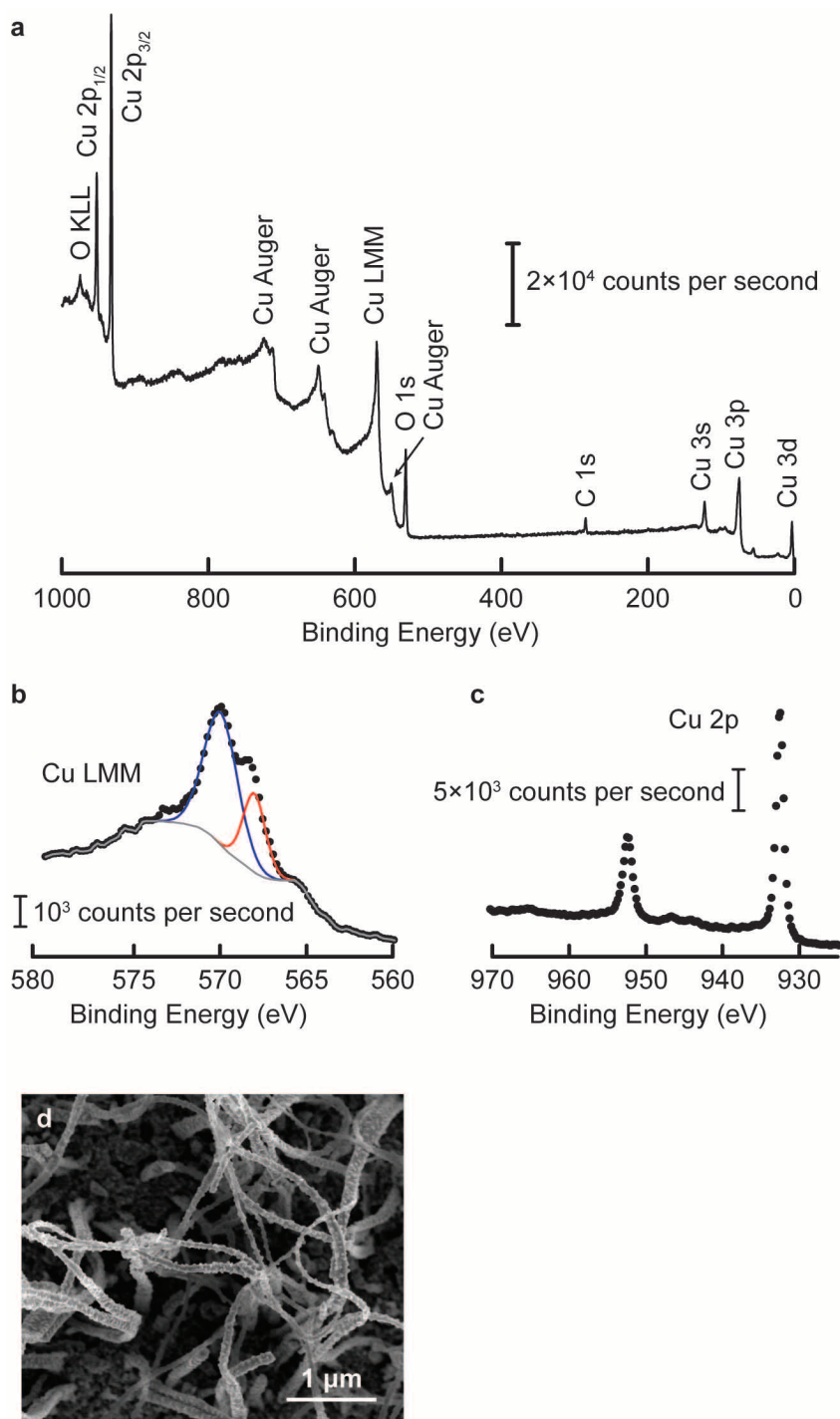
Ex situ analyses. Samples for *ex situ* analyses were removed from the electrolyte solution, rinsed gently with deionized water and allowed to dry under N_2 flow. TEM samples were prepared at the Evans Analytical Group and images were acquired at the National Center for Electron Microscopy. TEM-ready samples for OD-Cu 1 and OD-Cu 2 were prepared from a carbon ink coated area using an *in situ* focused-ion-beam lift-out technique on a FEI Strata 400 Dual Beam focused ion beam/SEM. The samples were imaged in a conventional FEI Titan 80-300 (S)TEM microscope and in a Transmission Electron Aberration-Corrected Microscope (TEAM 0.5) operated at 300 kV in bright-field TEM mode and high-resolution TEM mode. SEM images were acquired with an FEI Magellan 400 XHR Scanning Electron Microscope with field-emission-gun source. X-ray photoelectron spectra were obtained with a PHI VersaProbe II scanning X-ray photoelectron spectroscopy Microprobe. Grazing-incidence X-ray diffraction patterns were acquired at the Evans Analytical Group using a PANalytical X'Pert diffractometer with a Cu X-ray tube and parallel beam optics. All patterns were acquired at an incidence angle of 4°. Additional high-resolution grazing-incidence X-ray diffraction patterns for Williamson–Hall analysis were acquired at beamline 2-1 of the Stanford Synchrotron Radiation Lightsource using 11.5 keV X-rays with Soller slits and a photomultiplier tube detector.

Surface area determination. Surface roughness factors for the OD-Cu electrodes and Cu nanoparticle electrodes relative to polycrystalline Cu foils were determined

by measuring double layer capacitances³¹. Cyclic voltammetry was performed in the same electrochemical cell as in bulk electrolyses with a Nafion proton exchange membrane and 0.1 M HClO₄ electrolyte. The geometric current density at a potential at which no Faraday process was occurring was plotted against the scan rate of the cyclic voltammetry. The slope of the linear regression gives the capacitance. A

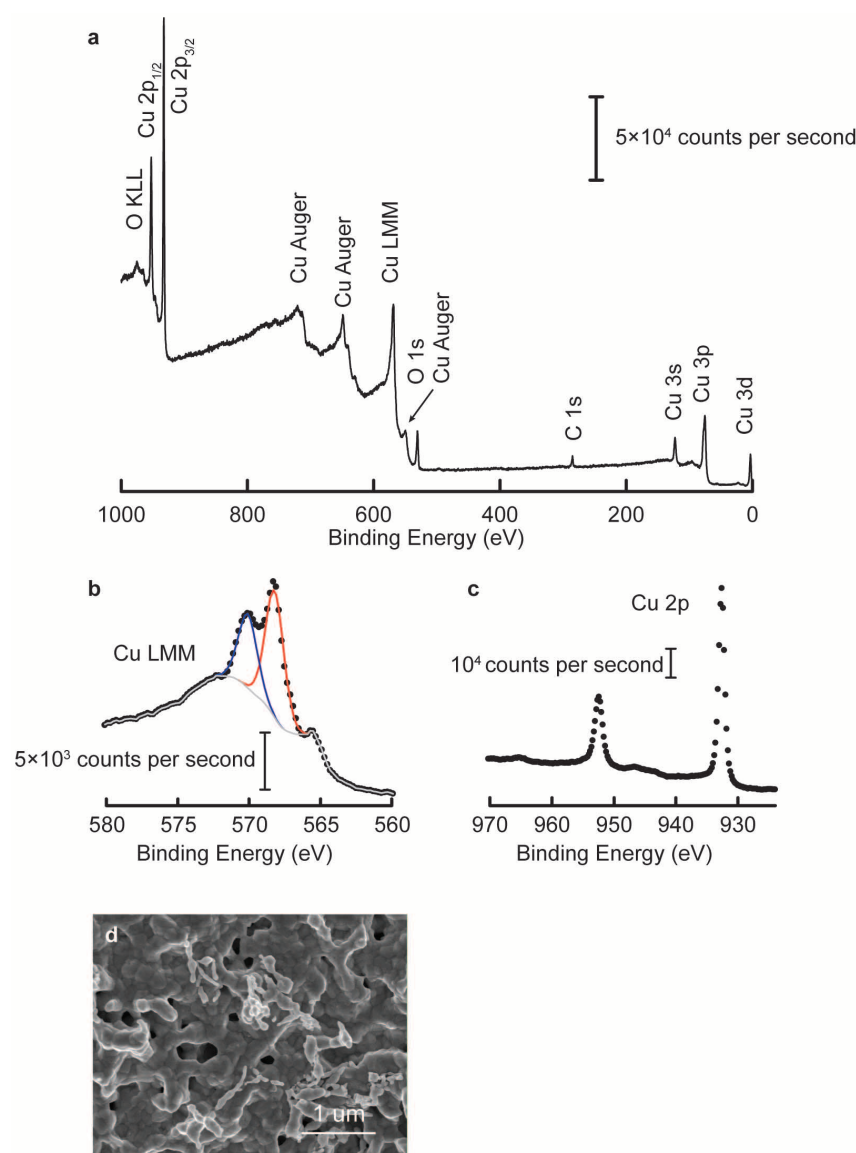
representative set of cyclic voltammeteries for OD-Cu 1 and OD-Cu 2 electrodes are shown (Extended Data Fig. 5).

31. Waszczuk, P., Zelenay, P. & Sobkowski, J. Surface interaction of benzoic-acid with a copper electrode. *Electrochim. Acta* **40**, 1717–1721 (1995).
32. CRC. *Handbook of Chemistry and Physics* 9th edn, section 5 (CRC, 2013).



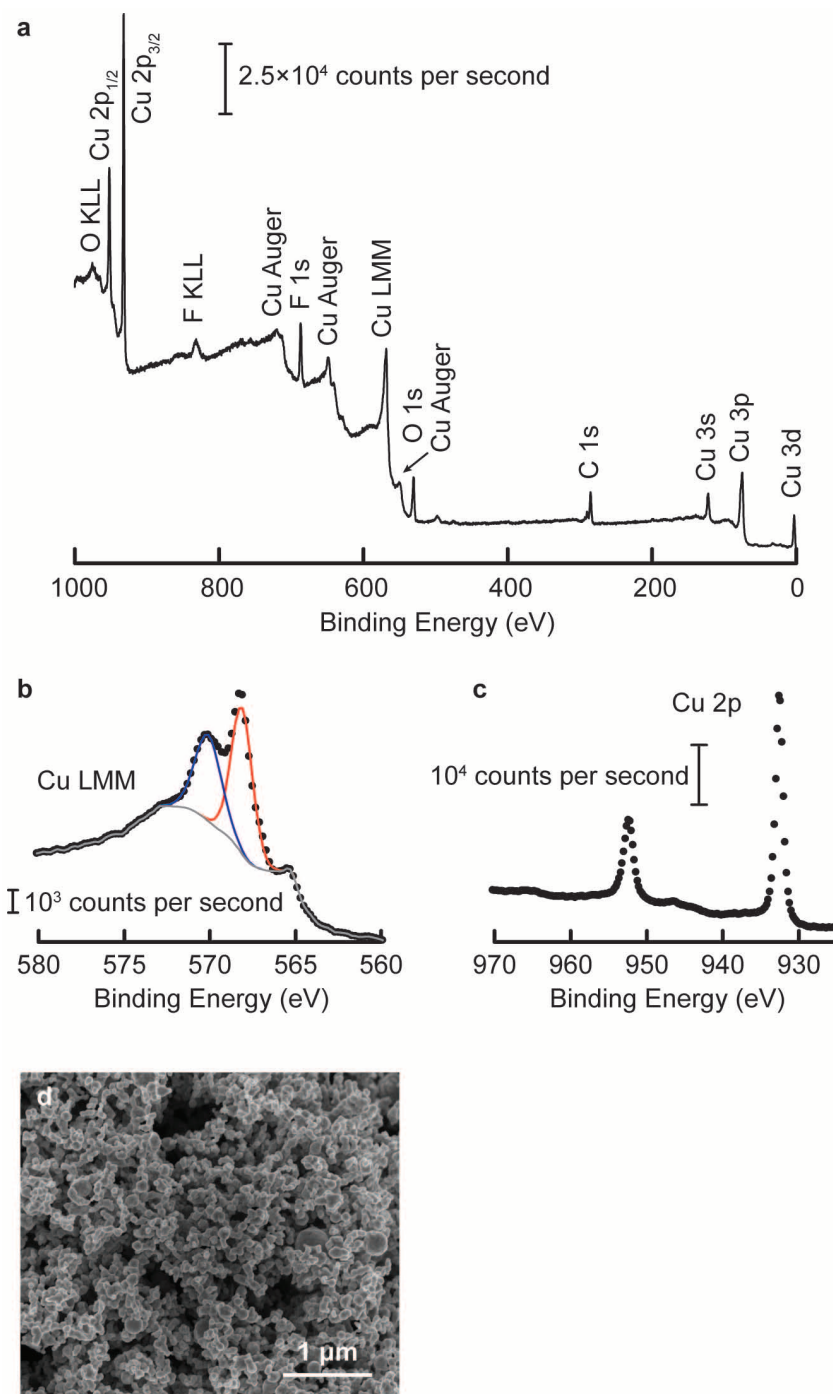
Extended Data Figure 1 | Additional physical characterization of OD-Cu 1.
a, X-ray photoelectron spectroscopy survey spectrum. **b**, High-resolution X-ray

photoelectron spectrum of the Cu LMM region. **c**, High-resolution X-ray photoelectron spectrum of the Cu 2p peaks. **d**, Low-resolution SEM image.



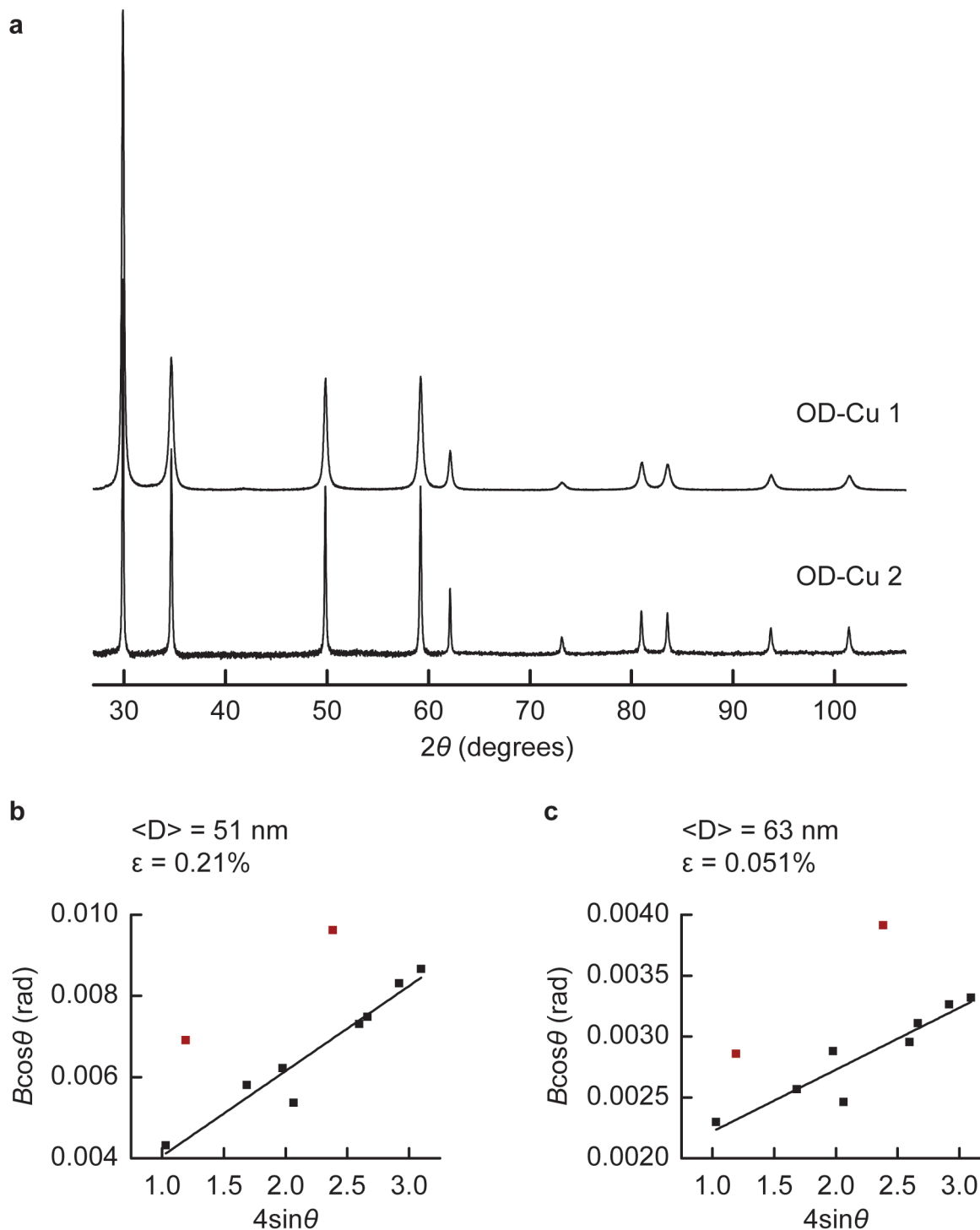
Extended Data Figure 2 | Additional physical characterization of OD-Cu 2.
a, X-ray photoelectron spectroscopy survey spectrum. **b**, High-resolution X-ray

photoelectron spectrum of the Cu LMM region. **c**, High-resolution X-ray photoelectron spectrum of the Cu 2p peaks. **d**, Low-resolution SEM image.



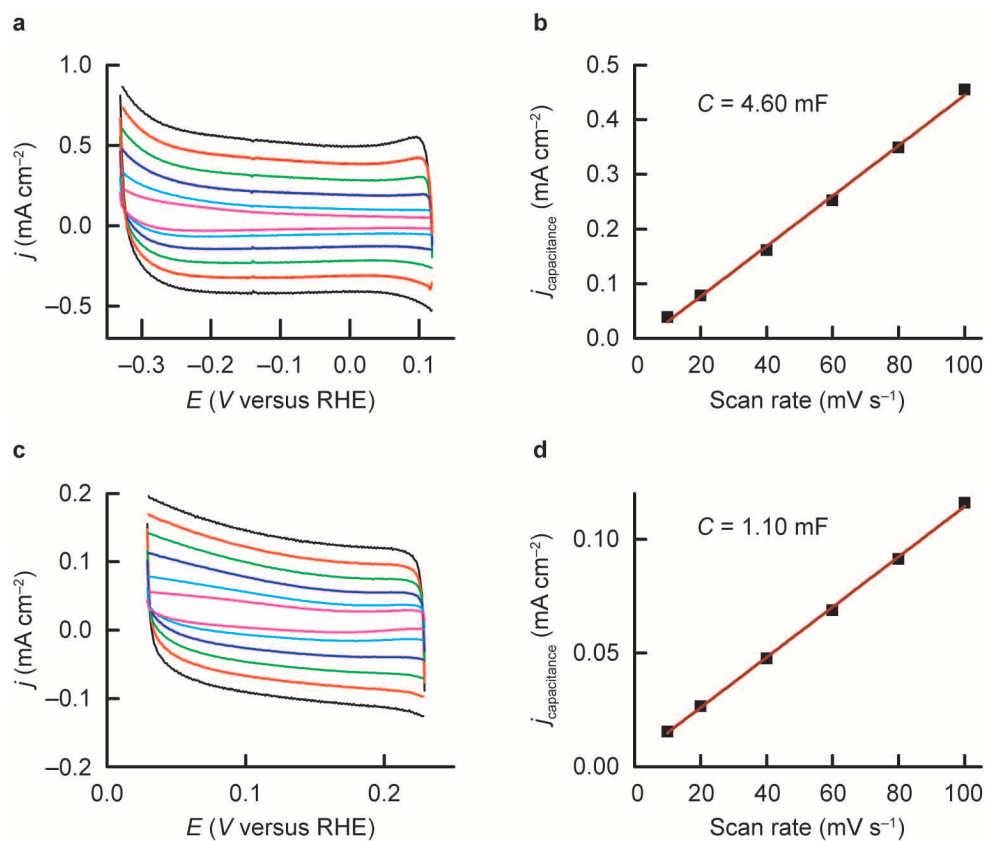
Extended Data Figure 3 | Additional physical characterization of Cu nanoparticle electrodes. **a**, X-ray photoelectron spectroscopy survey spectrum. **b**, High-resolution X-ray photoelectron spectrum of the Cu LMM

region. **c**, High-resolution X-ray photoelectron spectrum of the Cu 2p peaks. **d**, Low-resolution SEM image.



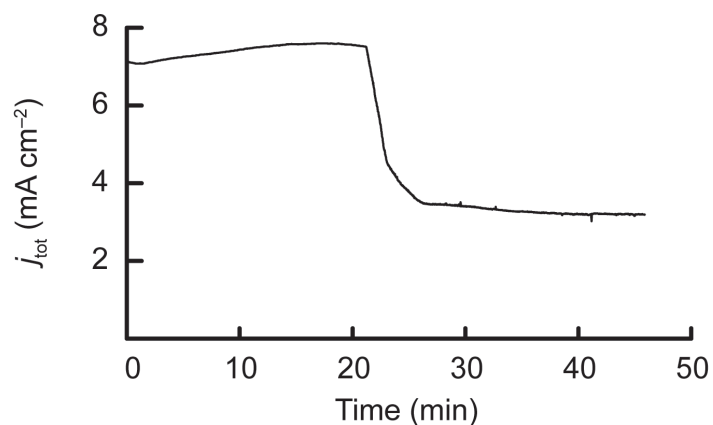
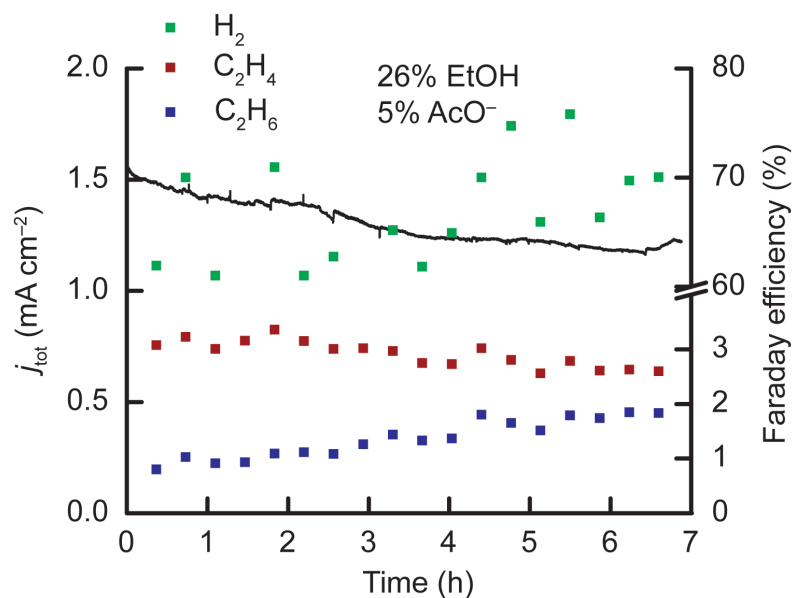
Extended Data Figure 4 | Additional grazing-incidence X-ray diffraction pattern data, collected using synchrotron X-rays at 11.5 keV. a, X-ray diffraction patterns for OD-Cu 1 and OD-Cu 2. b, c, Williamson-Hall plots for OD-Cu 1 (b) and for OD-Cu 2 (c), where B = integral breadth of the peak, and

the points highlighted in red have been excluded. To calculate crystallite size and strain, the following relationships were used: $B = K\lambda/\langle D \rangle \cos \theta + 4\varepsilon \tan \theta$, where $\langle D \rangle$ is the average crystallite size, λ is the wavelength, ε is the non-uniform strain (microstrain), and the Scherrer constant $K \approx 1$.



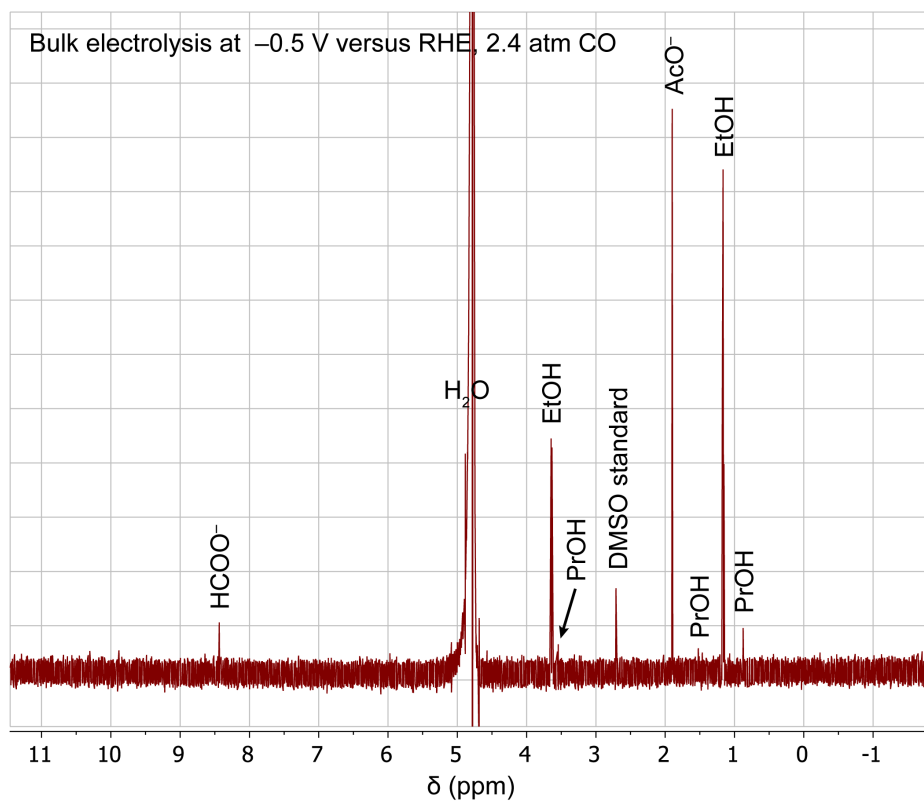
Extended Data Figure 5 | Electrochemical surface area measurement.
a, b, Determination of double-layer capacitance over a range of scan rates for an OD-Cu 1 electrode after 1 h bulk electrolysis. **c, d,** Determination of double-layer capacitance over a range of scan rates for an OD-Cu 2 electrode

after 12 h bulk electrolysis at -0.3 V versus RHE in 0.1 M KOH . **a, c,** Cyclic voltammograms taken over a range of scan rates. **b, d,** Current due to double-layer charging plotted against cyclic voltammetry scan rate.

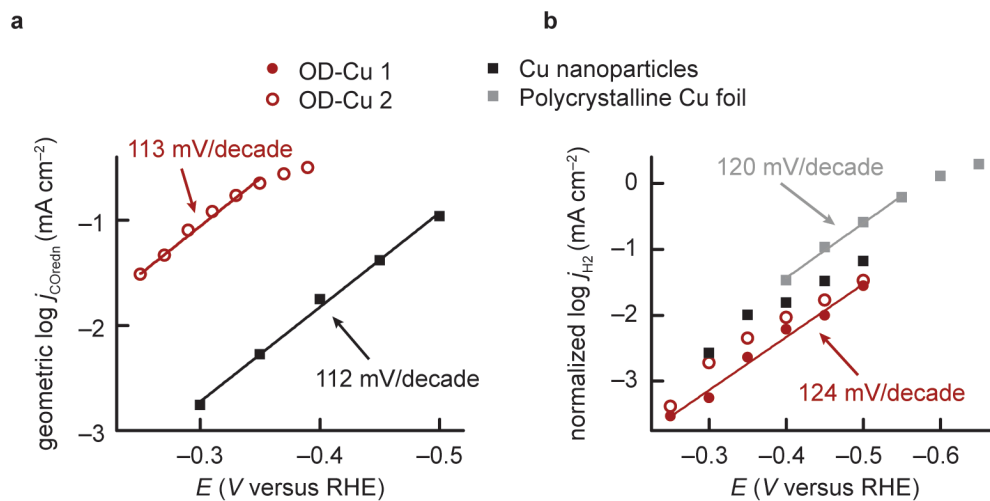
a Reduction of Cu_2O at -0.5 V versus RHE**b** Bulk electrolysis at -0.4 V versus RHE, 1 atm CO

Extended Data Figure 6 | Representative bulk-electrolysis data for CO reduction on OD-Cu 1. **a**, Current density over time for the reduction of Cu_2O to form active OD-Cu. **b**, Current density over time (left) for OD-Cu 1 at -0.4 V

versus RHE in 0.1 M KOH, saturated with 1 atm CO and Faraday efficiency over time (right) for H_2 (green), C_2H_4 (red), and C_2H_6 (blue). Efficiencies for EtOH and AcO^- were obtained at the end of the electrolysis.

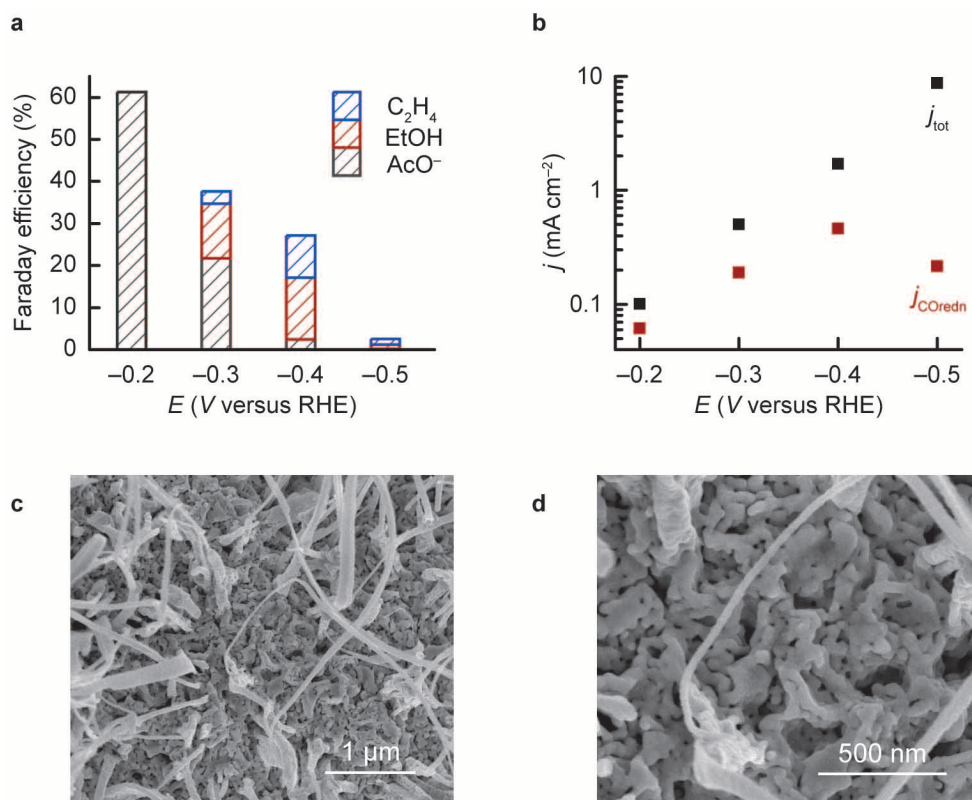


Extended Data Figure 7 | Representative NMR spectrum for an OD-Cu 1 bulk electrolysis at -0.5 V versus RHE in 0.1 M KOH, saturated with 2.4 atm CO. DMSO, dimethyl sulphoxide.



Extended Data Figure 8 | Additional Tafel data collected in 0.1 M KOH, saturated with 1 atm CO. **a**, Geometric current density for CO reduction versus potential for OD-Cu 2 and Cu nanoparticles. **b**, Surface-area-normalized

current density for H_2 evolution versus potential for OD-Cu 1, OD-Cu 2, Cu nanoparticles and polycrystalline Cu foil.



Extended Data Figure 9 | CO reduction bulk electrolysis data for OD-Cu 1 in 1 M KOH, saturated with 1 atm CO. **a**, Faraday efficiency for various products versus potential. **b**, Total current density and partial current density

for CO reduction versus potential. **c**, **d**, SEM images of OD-Cu 1 after electrolysis in 1 M KOH.

Extended Data Table 1 | Summary of CO reduction total geometric current densities and Faraday efficiencies for OD-Cu and Cu nanoparticle electrodes

<i>E</i> versus RHE V	<i>j</i> _{tot} mA cm ⁻²	Faraday Efficiency / %				
		AcO ⁻	EtOH	PrOH	C ₂ H ₄	C ₂ H ₆
OD-Cu 1 in 0.1 M KOH, saturated with 1 atm CO						
-0.25	0.0922	17.9	32.5	0.0	0.0	0.0
-0.30	0.285	13.6	42.9	0.0	0.6	0.0
-0.35	0.626	6.8	35.8	0.0	1.2	0.0
-0.40	1.30	3.5	26.1	0.0	3.2	0.5
-0.45	2.07	2.0	18.9	0.0	3.1	1.0
-0.50	3.03	1.1	12.8	0.0	4.6	0.7
OD-Cu 1 in 0.1 M KOH, saturated with 2.4 ± 0.07 atm CO.						
-0.30	0.600	16.8	32.7	0.0	0.0	0.0
-0.35	1.28	14.3	33.2	0.0	0.0	0.0
-0.40	1.95	11.6	28.1	0.0	0.3	0.7
-0.45	2.79	10.3	28.7	0.0	0.7	1.3
-0.50	4.43	5.6	20.5	3.0	1.4	1.8
OD-Cu 2 in 0.1 M KOH, saturated with 1 atm CO						
-0.25	0.0432	17.3	13.7	0	0	0
-0.30	0.180	13.8	25.5	0	0	0
-0.35	0.416	12.8	30.4	0	0.69	1.1
-0.40	0.812	6.9	25.7	10.0	3.5	2.5
-0.45	1.22	1.7	15.1	5.0	4.8	1.4
-0.50	1.78	0.75	15.2	2.2	10.8	0.37
Cu nanoparticles in 0.1 M KOH, saturated with 1 atm CO						
-0.30	0.031	5.7	0.0	0.0	0.0	0.0
-0.35	0.121	2.1	2.3	0.0	0.0	0.0
-0.40	0.302	2.0	3.7	0.0	0.0	0.0
-0.45	0.653	0.4	5.2	0.0	0.7	0.0
-0.50	1.95	0.4	2.7	0.0	2.4	0.0
-0.60	3.97	0.1	0.6	1.1	1.9	0.0

The remainder of the current is attributed to H₂ evolution.

Extended Data Table 2 | Capacitance values and surface roughness factors measured using cyclic voltammetry for selected electrodes discussed in this report

Electrode preparation	Capacitance	Surface roughness factor
Polycrystalline Cu	29 μF	1
Cu nanoparticles	0.77–0.96 mF	26–33
OD-Cu 1, after 1 h bulk electrolysis	4.6–4.8 mF	159–167
OD-Cu 1, after 12 h bulk electrolysis	3.0–3.2 mF	102–111
OD-Cu 2, after 1 h bulk electrolysis	1.8 mF	62
OD-Cu 2, after 12 h bulk electrolysis	1.1 mF	39

The surface roughness factor for electropolished polycrystalline Cu is defined to be 1.